Effect of Alloying Additions on Microstructure, Mechanical and Magnetic Properties of Rapidly Cooled Bulk Fe-B-M-Cu (M = Ti, Mo and Mn) Alloys

MARIUSZ HASIAK ⓘ, MARZENA TKACZYK, AMADEUSZ ŁASZCZ ⓘ, and JACEK OLSZEWSKI ⓘ

The influence of alloying additions on the microstructure, mechanical, and magnetic properties of bulk $Fe_{79}B_{20}Cu_1$, $Fe_{79}B_{16}Ti_4Cu_1$, $Fe_{79}B_{16}Mo_4Cu_1$ and $Fe_{79}B_{16}Mn_4Cu_1$ (at. pct) alloys was investigated. Nanocrystalline samples in the form of 3 mm rods were prepared directly by suction casting without additional heat treatment. Mössbauer spectroscopy, transmission electron microscopy and scanning electron microscopy studies confirmed that the investigated alloys consist α-Fe and Fe_2B nanograins embedded in an amorphous matrix. The addition of alloying elements, such as Ti, Mo and Mn to $Fe_{79}B_{20}Cu_1$ alloy increases the amount of amorphous phase and decreases the presence of Fe_2B phase in all examined alloys. The mechanical properties of the samples, such as hardness, elastic modulus, and elastic energy ratio, were analysed by an instrumented indentation technique performed on a 12×12 nanoindentation grid. These tests allowed to characterise the mechanical properties of the regions observed in the same material. For the $Fe_{79}B_{20}Cu_1$ alloy, the hardness of 1508 and 1999 HV, as well as Young's modulus of 287 and 308 GPa, were estimated for the amorphous- and nanocrystalline-rich phase, respectively. The addition of Ti, Mo, and Mn atoms leads to a decrease in both hardness and elastic modulus for all regions in the investigated samples. Investigations of thermomagnetic characteristics show the soft magnetic properties of the studied materials. More detailed studies of magnetisation versus magnetic field curves for the $Fe_{79}B_{20-x}M_xCu_1$ (where $x = 0$ or 4; M = Ti, Mo, Mn) alloy, recorded in a wide range of temperatures, followed by the law of approach to magnetic saturation revealed the relationship between microstructure and magneto-mechanical properties.

I. INTRODUCTION

RAPID solidification techniques, such as melt spinning and suction casting, are based on high cooling rates. The critical cooling rate depends on the chemical composition of the alloy, and for Fe-based alloys, a cooling rate of about 10^6 K/s is required to produce amorphous ribbons 20-25 μm thick.[1–6] Nowadays, many novel amorphous alloys such as Zr-, Pd-, Pt-based materials are produced with critical cooling rates below 100 K/s. The thickness of the manufactured materials exceed 1 mm,[7,8] and the optimised manufacturing process leads to the obtaining of amorphous materials in the form of sheets,[9] wires,[10] and rods.[11] Fe-based amorphous alloys manufactured by rapid cooling techniques have received great attention because of their unique combination of mechanical and magnetic properties. Depending on their chemical composition, they are characterised by excellent mechanical properties such as elevated ultimate tensile[11,12] and compression strength,[13,14] enhanced hardness,[15] and good soft magnetic properties.[15–18] In comparison with their coarse-grained crystalline counterparts. Nanocrystalline Fe/Co-based ferromagnetic composites are predominantly produced by isothermal annealing of the amorphous precursor at a temperature slightly above the primary crystallisation temperature. The nanocrystalline materials manufactured by this technique are usually produced in the form of ribbons and have a structure consisting of nanosized grains immersed in an amorphous matrix.[19–21] They exhibit even higher soft

MARIUSZ HASIAK and AMADEUSZ ŁASZCZ are with the Department of Mechanics, Materials and Biomedical Engineering, Wrocław University of Science and Technology, Smoluchowskiego 25, 50-370 Wroclaw, Poland. mariusz.hasiak@pwr.edu.pl. MARZENA TKACZYK is with the Laboratory for In-situ Microscopy & Analysis, Department of Engineering Science, University of Oxford, Parks Road, Oxford, OX1 3PJ, UK. JACEK OLSZEWSKI is with the Institute of Physics, Częstochowa University of Technology, Al. Armii Krajowej 19, 42-200 Częstochowa, Poland.

magnetic properties, that is, high permeability, high saturation flux density, and low coercivity compared to amorphous alloys.[22–24] The excellent soft magnetic properties arise from the great reduction in the mean magnetocrystalline anisotropy. The predominant achievement of a crystalline structure in amorphous alloys leads to a decrease in their mechanical parameters.[25–27] However, optimal manufacturing parameters allow for the production of bulk metallic glasses matrix composites (BMGMCs) that combine amorphous and nanocrystalline structures.[28–30] Depending on the manufacturing parameters, these microstructures precipitate in the form of dendrites[31–36] or nanoeutectics.[37–41] During this one-step process, the nanocrystalline phase precipitates directly from the liquid state (*in situ* process), whereas the remaining matrix solidifies in an amorphous phase.[28,36,42] Thus, it is possible to produce the amorphous-nanocrystalline composite directly in the casting process without any subsequent problematic heat treatment. This manufacturing approach was reported for Zr-based,[34,43,44] Ti-based,[45–47] Mg-based,[48–50] and finally Fe-based[35,36,38,40] alloys. The BMGMCs are characterized by superior mechanical properties in comparison with their amorphous counterparts, *i.e.,* enhanced hardness,[30,51] plastic deformation,[35,37,52] compressive strength[51–53] and fracture toughness.[35,54,55] It was reported in several articles that the mechanical and magnetic properties of the manufactured materials are closely related to their microstructure.[30,56–61] Bulk amorphous and nanocrystalline alloys, due to their unique mechanical and/or magnetic properties, are of considerable interest in modern sections of industries, e.g., arms industry,[62] electrotechnical industry, biomedicine and nanotechnology.[63] In recent years, great emphasis has been placed on energy-efficient applications and the reduction of energy losses. Therefore, amorphous/nanocrystalline Fe-based alloys are considered in various applications such as magnetic cores and magnetic screens.[64–66]

The aim of this paper was to manufacture novel, low-cost[9,67] nanocrystalline $Fe_{79}B_{20-x}M_xCu_1$ (where x = 0 or 4; M = Ti, Mo, Mn) bulk alloys directly in the casting process without performing additional heat treatment. Comprehensive studies of the relationship of microstructure to mechanical and magnetic properties were performed in a wide range of mechanical loads, temperature, and magnetic fields.

II. EXPERIMENTAL PROCEDURES

Alloy ingots with a nominal composition of $Fe_{79}B_{20}Cu_1$, $Fe_{79}B_{16}Ti_4Cu_1$, $Fe_{79}B_{16}Mo_4Cu_1$, and $Fe_{79}B_{16}Mn_4Cu_1$ (at. pct) were prepared from a FeB-base alloy and pure elements by an arc melting technique in a high-purity argon atmosphere. All ingots were remelted five times to obtain a homogeneous structure. The compositions of the alloys were chosen based on the composition rules for obtaining amorphous structures[68,69]: (a) the alloys must consist of more than three elements, (b) the difference in the atomic size ratios of the elements must be greater than

12 pct, and (c) the main constituent elements must have negative heats of mixing between themselves. Furthermore, the composition principles of commercial nanocrystalline NANOPERM-type alloys with the addition of 1 at. pct copper were also followed.[20,70] The alloying elements used in this paper, such as Mn,[71] Ti,[72] and Mo,[73] are also known for stabilising the amorphous phase in ultra-fast cooled Fe-based alloys. Cylindrical rods with a diameter of 3 mm were fabricated by suctioning the molten alloy into a copper mold. A schematic diagram of the arc melter with suction casting option used to manufacture the samples, together with the example of the produced material, is presented in Figure 1. The following manufacturing parameters were used to produce samples in the form of rods: current—350 A, suction pressure—950 hPa. Based on data from the References 74 and 75, the estimated cooling rate was about 450 K/s. All samples for microstructural observations were prepared by cutting 3 mm in diameter rods with the help of Electrical Discharge Machining, following two-sided mechanical polishing.

The structure of all manufactured samples was examined by a PANalytical X'Pert Pro X-ray diffractometer using Cu K_α radiation. The XRD patterns of the studied samples can be found in Reference 76.

Surface observations of the $Fe_{79}B_{20}Cu_1$, $Fe_{79}B_{16}Ti_4Cu_1$, $Fe_{79}B_{16}Mo_4Cu_1$, and $Fe_{79}B_{16}Mn_4Cu_1$ alloys were carried out on a Carl Zeiss Evo LS15 variable pressure scanning electron microscope (SEM), equipped with a LaB_6 gun source and a range of detectors for electron imaging. All observations were carried out with a backscattered electron (BSE) detector at an accelerating voltage of 15 kV and a working distance of 10 mm. Moreover, the chemical composition of the produced alloys was also analysed by an energy dispersive spectroscopy detector (EDS).

Images in bright and dark fields and diffraction patterns from various regions were obtained by a JEOL JEM-3010 transmission electron microscope (TEM) to verify the presence of nanocrystalline and amorphous
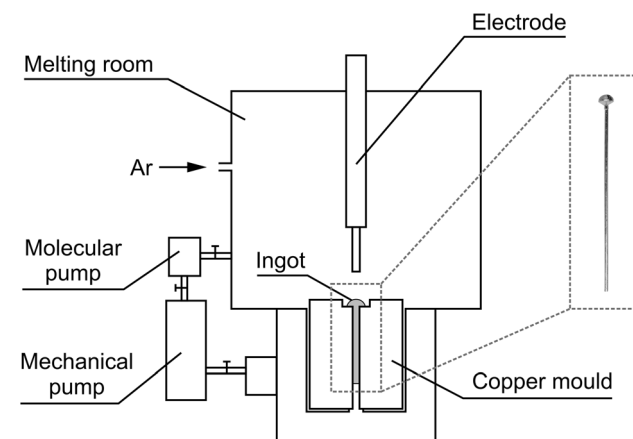

Fig. 1—Schematic diagram of the arc melting and suction casting apparatus and an example of the cast rod (dashed insert).

phases in the examined materials. All investigations were performed for samples prepared in the form of thin foil by mechanical and electrolytic polishing.

The Mössbauer spectra were measured at room temperature in transmission geometry using a conventional Mössbauer spectrometer working at a constant acceleration with the ^{57}Co(Rh) radioactive source of the 1.8 GBq in activity. The calibration of the spectrometer was performed for 0.02 mm thick α-Fe foil. The samples for measurements were prepared in the form of thin plates of about 0.02 mm. The spectra were fitted using the Normos package[77] with a thin absorbent approximation. Moreover, the Lorentzian shape of the emission and absorption lines as well as the probability of recoil-free emission and absorption of γ-rays from nuclear transitions were assumed to be the same for all Fe atoms in the sample.

The mechanical properties of the produced $Fe_{79}B_{20-x}M_xCu_1$ (where $x = 0$ or 4; M = Ti, Mo, Mn) alloys were evaluated using the Nanoindentation Tester (NHT^2, CSM Instruments) equipped with Berkovich indenter. The 144 nanoindentation tests were carried out with a maximum load of 50 mN for each specimen. The load/unload rate was 100 mN/min, and the dwell time at maximum load was 10 seconds. In these studies, a constant value of Poisson's ratio equal to 0.3 was assumed for all investigated alloys. The instrumental Vickers hardness, Young's elastic modulus, and deformation energy were determined according to the Oliver–Pharr procedure.[78] Statistical analysis of the obtained results was performed to separate the mechanical properties of each phase in the manufactured alloys.

The thermomagnetic characteristics of the produced materials were examined by a Vibrating Sample Magnetometer (VSM) (PPMS, Quantum Design) in a wide range of temperature and external magnetic fields. Isothermal DC hysteresis loops were recorded in the temperature range from 50 to 400 K with the step of 50 K for a maximum external magnetic field up to 1200 kA/m. The effective magnetocrystalline anisotropy constant (K_{eff}) was calculated from the initial magnetisation curves based on the law of approach to saturation magnetisation.

III. RESULTS AND DISCUSSION

A. Investigations of Microstructure

It is well known that microstructure affects the physical properties of the investigated materials. Therefore, in this work, the authors present the results of microstructure studies carried out using various research techniques. Mössbauer spectra and the corresponding magnetic hyperfine field distributions for the as-cast $Fe_{79}B_{20}Cu_1$, $Fe_{79}B_{16}Ti_4Cu_1$, $Fe_{79}B_{16}Mo_4Cu_1$ and $Fe_{79}B_{16}Mn_4Cu_1$ alloys, obtained by employing the Hesse-Rübartsch method,[79] are presented in Figure 2. The open circles in Mössbauer spectra represent experimental data, while the solid lines represent theoretically matched lines [Figures 2(a) to (d)]. All experimental spectra were decomposed into elementary sextets with

different line intensities and half width. One sextet was assigned to α-Fe (red color), two sextets to ordered and one sextet to non-ordered or highly defected Fe_2B phase (green color),[80] and the sum of 36 sextets to amorphous phase (blue color). For the $Fe_{79}B_{20}Cu_1$, $Fe_{79}B_{16}Mo_4Cu_1$ and $Fe_{79}B_{16}Mn_4Cu_1$ alloys, the addition of a broadened single line (purple color) assigned to the part of the amorphous phase with Fe atoms with vanishing hyperfine interactions was necessary to receive good agreement with the experimental data. It suggests that part of the interaction between Fe atoms in these materials occurs through a paramagnetic matrix. Moreover, all of these alloys include only one component, which is assigned to the non-ordered or highly defected Fe_2B phase. The Ti-containing alloy exhibits completely different behavior, and this material did not show the
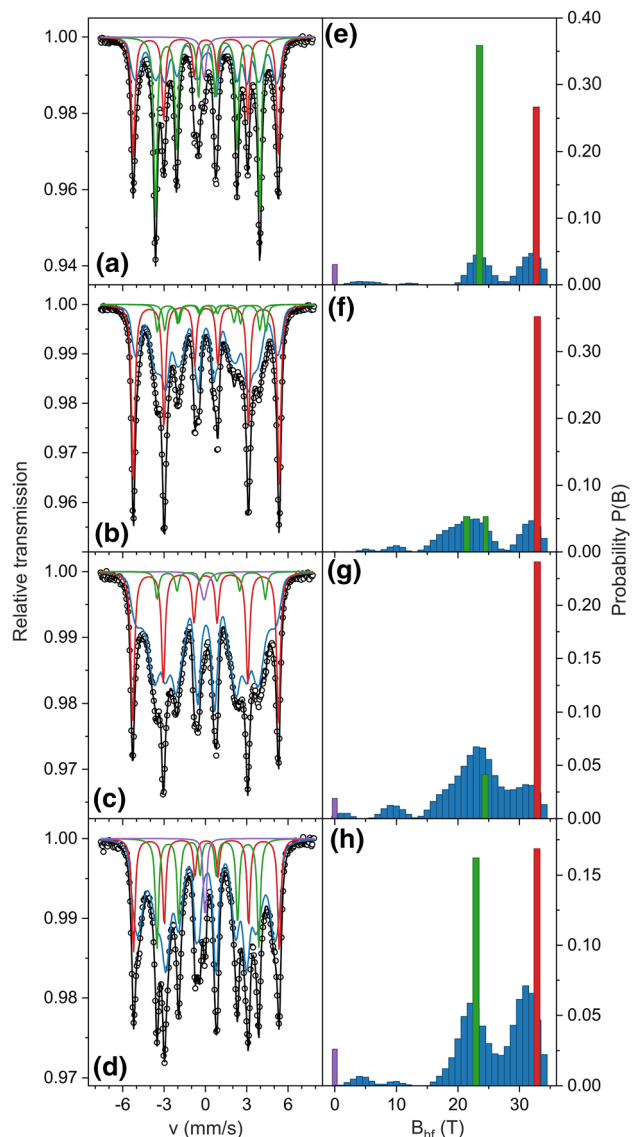

Fig. 2—Mössbauer spectra (a) to (d) and corresponding hyperfine field distributions (e) to (h) of the as-cast $Fe_{79}B_{20}Cu_1$ (a, e), $Fe_{79}B_{16}Ti_4Cu_1$ (b, f), $Fe_{79}B_{16}Mo_4Cu_1$ (c, g) and $Fe_{79}B_{16}Mn_4Cu_1$ (d, h) alloys. Blue/purple color corresponds to the amorphous phase, red to α-Fe phase, and green to Fe_2B phase (Color figure online).

presence of paramagnetic subspectra. On the other hand, two components were found assigned to the ordered Fe_2B phase (green lines) with different Fe/B atoms were found [Figures 2(b), (f)].

The results obtained from the numerical analysis of the recorded Mössbauer spectra are summarised in Table I and Figure 3. The hyperfine field distributions [Figures 2(e) to (h)] obtained from the numerical analysis of the Mössbauer spectra [Figures 2(a) to (d)] show the complex arrangements of Fe atoms in the investigated materials. It is well seen that all of the manufactured materials in the as-cast state were partially crystallised. The red component, related to α-Fe phase, is on $P(B_{hf})$ [Figures 2(e) to (h)] allocated close to 33 T. The different values of B_{hf} (Table I) are related to the small precipitation of alloying atoms (probably B atoms) in this phase. Assuming identical partial atomic volumes for alloying elements, one can estimate volume fractions of crystalline phases (Table I), and the rest is the volume fraction of the amorphous matrix. The volume fraction of the amorphous phase for the $Fe_{79}B_{20}Cu_1$ alloy is equal to 40 pct, whereas the addition of alloying elements leads to an increase in the amorphous matrix to 60, 77 and 65 pct for the Ti-, Mo- and Mn containing samples, respectively (Figure 3). The corresponding multicomponents distribution in $P(B)$ (marked by blue/purple color) for the amorphous phase in the $Fe_{79}B_{20}Cu_1$ alloy [Figure 1(e)] suggests a non-uniform arrangement of Fe atoms in the amorphous matrix. The same behavior was also observed for the other investigated samples [Figures 1(f) to (h)]. It confirms that during rapid cooling of alloys from liquid to solid state, Fe atoms are frozen, and high internal stresses are generated.[81–83] Stress relief annealing below the crystallisation temperature leads to a reduction of free volumes in the materials and improvement of physical properties. It is worth emphasising that the alloying elements lead to a decrease in the volume fraction of the Fe_2B phase in the as-cast $Fe_{79}B_{20}-xM_xCu_1$ (where $x = 0$ or 4; M = Ti, Mo, Mn) alloys.

The microstructure of the nanocrystalline $Fe_{79}B_{20-x}M_xCu_1$ (where $x = 0$ or 4; M = Ti, Mo, Mn) bulk alloys was also analysed in nano- and micro-scale using TEM and SEM, respectively. An example of a TEM image for the $Fe_{79}B_{20}Cu_1$ alloy is presented in Figure 4. It is seen that three different regions are present in the investigated sample. The same microstructures consisting of nanocrystalline grains embedded in the amorphous matrix were also observed for other produced materials. The amorphous phase [Figure 4(b)] is located mainly near the edges of the sample. The corresponding diffraction pattern with characteristic blurred rings is shown in Figure 4(b) as an inset. The TEM observations also show the presence of a nanocrystalline structure. A more detailed analysis of the diffraction pattern, attached to Figure 4(c), confirms that the visible nanocrystalline grains with a size of approximately 20 nm correspond to α-Fe grains.[76] The existence of Fe_2B crystallites precipitated in the production process is depicted in Figure 4(d). The

results obtained from the TEM analysis are in accordance with the Mössbauer data presented in Table II.

Figure 5 shows backscattered SEM images recorded in a micro scale for the $Fe_{79}B_{20}Cu_1$, $Fe_{79}B_{16}Ti_4Cu_1$, $Fe_{79}B_{16}Mo_4Cu_1$ and $Fe_{79}B_{16}Mn_4Cu_1$ alloys. The various concentrations of atoms in the investigated samples are visible as regions with different grayscale. During the rapid quenching process, some atoms agglomerate mainly in the centre of the rods, leading to the formation of different types of dendrites and eutectics structures. The size and form of the created structures (Figure 5) are strongly dependent on the chemical composition of the produced bulk materials. It involves the physical properties of the alloys, such as thermal conductivity, heat capacity, and viscosity. The energy-dispersive X-ray spectroscopy analysis confirmed that the dark regions mainly consist of Fe and B atoms in a ratio corresponding to the Fe_2B phase, while the remaining bright regions varied in atomic composition.[76] What is significant, Cu atoms, which play a dominant role in the crystallisation process of FINEMET alloys, were found primarily in bright areas. It should be noted that the $Fe_{79}B_{20}Cu_1$ alloy with a 60 pct amorphous + α-Fe phase (Table I, Figure 3) shows a higher amount of Fe_2B than samples with alloying additions. The addition of Ti, Mo and Mn leads to microstructure refinement, which is well seen by the comparison of $Fe_{79}B_{20}Cu_1$ alloy [Figure 5(a)] with Ti-, Mo- and Mn-containing samples [Figures 5(b) to (d)]. The images obtained from the SEM presented in Figure 5 are in good agreement with the Mössbauer data shown in Table I. The alloying additions affect the microstructure of $Fe_{79}B_{20-x}M_xCu_1$ (where $x = 0$ or 4; M = Ti, Mo, Mn) bulk alloys by improving the amorphicity and decreasing the amount of Fe_2B phase.

B. Mechanical Properties

The mechanical properties of the produced materials were investigated using the instrumented nanoindentation technique. In a traditional hardness test, the measurement output is a single hardness value estimated based on the penetration depth and the maximum value of the applied static load. On the contrary, the instrumented indentation technique allows for a continuous recording of the displacement of the indenter (h) and the currently applied load (F) during the loading and unloading part of the measurement [Figure 6(a)]. As a result, the standard output of this measurement is a characteristic load-displacement curve, $F(h)$, presented in Figure 6(b). The subsequent analysis of the recorded curve makes it possible to estimate both the plastic and elastic properties of the investigated material. The most popular and widely used method to extract mechanical parameters from the $F(h)$ curve is the Oliver and Pharr procedure.[78] The approach proposed by Oliver and Pharr was also applied in this study.

The main physical assumption of the Oliver and Pharr approach is that deformation during the loading part is governed by both elastic and plastic processes. In contrast, the deformation during the unloading part is

Table I. The Average Hyperfine Magnetic Field for α-Fe and Fe₂B Phases (B_{hf}), the Average Hyperfine Magnetic Field of Low Field and High Field Components for the Amorphous Matrix (B_{am} and D_{am}), the Atomic Fraction of Iron Content in the Amorphous and Crystalline Phases (Fe and C_{Fe}), the Intensity of Spectra (Int), and the Atomic Fraction of the Phases (V) Obtained From the Numerical Analysis of the $Fe_{79}B_{20-x}M_xCu_1$ (where $x = 0$ or 4; M = Ti, Mo, Mn) alloys

Phase/Alloy	$Fe_{79}B_{20}Cu_1$	$Fe_{79}B_{16}Ti_4Cu_1$	$Fe_{79}B_{16}Mo_4Cu_1$	$Fe_{79}B_{16}Mn_4Cu_1$
α-Fe Phase				
B_{hf} (T)	32.72(3)	32.878(4)	32.88(2)	32.84(2)
C_{Fe} (Pct)	98	99	99	99
Int	0.250	0.320	0.225	0.160
V	0.2	0.25	0.18	0.13
Fe₂B Phase				
B_{hf} (T)	23.512(6)	21.43(3)	24.41(5)	22.93(2)
		24.50(3)		
Int	0.336	0.049	0.039	0.150
		0.049		
V	0.4	0.15	0.05	0.22
Amorphous Phase				
B_{am} (T)	26.1(3)	23.4(2)	23.0(2)	25.6(1)
D_{am} (T)	7.2(3)	6.7(1)	6.6(2)	6.4(1)
Int	0.386	0.582	0.720	0.670
Fe (Pct)	83	69.6	75.5	74
V	0.4	0.6	0.77	0.65
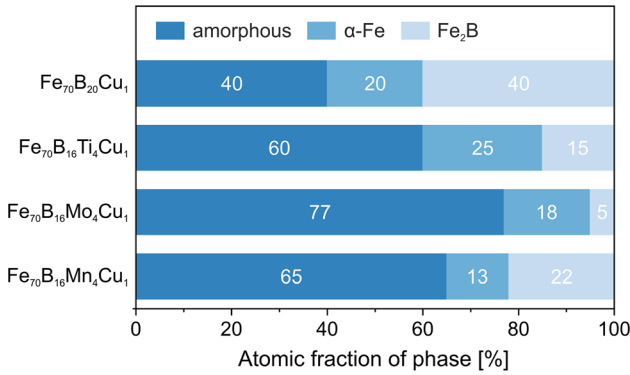
Fig. 3—Fraction of the amorphous α-Fe and Fe₂B phase in $Fe_{79}B_{20}Cu_1$, $Fe_{79}B_{16}Ti_4Cu_1$, $Fe_{79}B_{16}Mo_4Cu_1$ and $Fe_{79}B_{16}Mn_4Cu_1$ alloys.

elastic in nature only. The significant quantities characterising the load-displacement curve presented in Figure 6 are the maximum load F_{max}, the maximum displacement h_{max}, the final depth h_f, and the elastic unloading stiffness (or contact stiffness) $S = dF/dh$ estimated as the slope of the initial part of the unloading curve. It can be seen in Figure 6(c), that the indenter displacement (h_{max}) at the maximum load does not represent the actual contact deformation during loading due to the characteristic elastic sink-in. Considering this, the corrected contact depth (h_c) along which the indenter is in complete contact with a sample is defined as:

$$h_c = h_{max} - \varepsilon \frac{F_{max}}{S} \quad [1]$$

where ε is a geometry dependent parameter and equals $\varepsilon = 0.75$ for the Berkovich indenter.

The estimated h_c is used to compute the projected contact area A using the area function, which strictly depends on the shape of the indenter and must be carefully calibrated before measurement to compensate for any deviation from the nonideal geometry of the indenter. In the following study, the Berkovich tip geometry was fitted to the area function defined as:

$$A = C_0h_c^2 + C_1h + C_2h_c^{\frac{1}{2}} + C_3h_c^{\frac{1}{4}} + C_4h_c^{\frac{1}{8}} + C_5h_c^{\frac{1}{16}} + C_6h_c^{\frac{1}{32}} + C_7h_c^{\frac{1}{64}} \quad [2]$$

The determined contact area A is subsequently used to calculate the instrumented hardness H_{IT} from the following relation:

$$H_{IT} = \frac{F_{max}}{A} \quad [3]$$

Regarding the elastic properties of the sample, the indentation response during unloading is characterised by a reduced elastic modulus E_r determined from:

$$E_r = \frac{1}{2\beta}\frac{\sqrt{\pi}}{\sqrt{A}}S \quad [4]$$

where β represents the dimensionless correction factor. The reduced elastic modulus contains information about the elastic properties of both the sample and the indenter and combines this relation through the following equation:

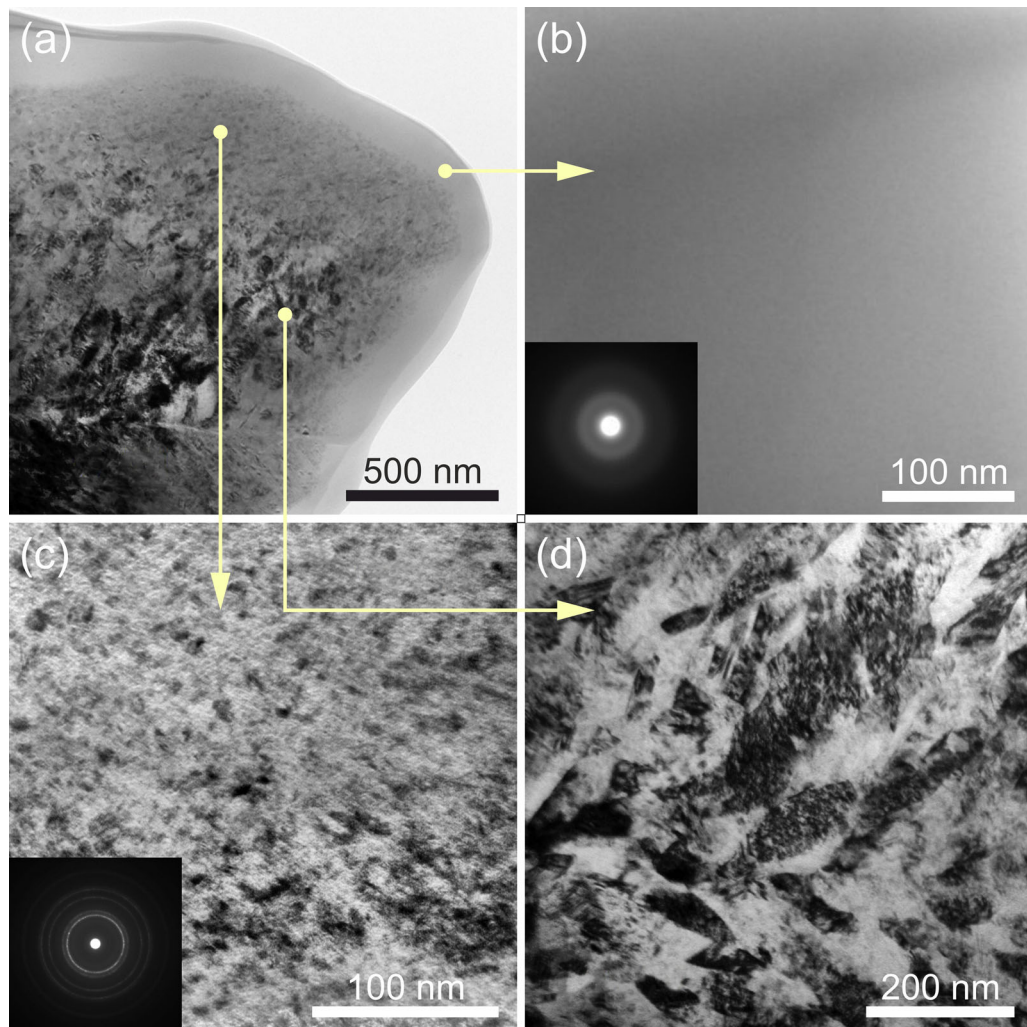$$\frac{1}{E_r} = \frac{1 - v_i^2}{E_i} + \frac{1 - v_s^2}{E_s} \quad [5]$$

Fig. 4—Example of TEM images of the $Fe_{79}B_{20}Cu_1$ alloy: (*a*) different characteristic regions of the nanocrystalline sample, (*b*) amorphous phase with characteristic halo recorded in the diffraction pattern, (*c*) α-Fe nanocrystalline grains embedded in the amorphous matrix and corresponding diffraction pattern of body-centred cubic Fe, (*d*) Fe_2B nanograins.

where E_s and n_s are the elastic modulus and Poisson's ratio of the sample, respectively. E_i and n_i are the elastic modulus and the Poisson's ratio of the indenter tip, respectively. Assuming that E_i and n_i for the diamond indenter are well defined, the above equation allows calculating Young's elastic modulus for the investigated sample.

The plastic and elastic energies during indentation are estimated as an area below the corresponding loading and unloading branch of the $F(h)$ curve, which is schematically depicted in Figure 6(b). The fraction of energy recovered during the unloading process (W_{elast}/W_{total}), determined by dividing the elastic energy (W_{elast}) by the total indentation energy ($W_{elast} + W_{plast}$), is also used in this study to characterise the investigated materials.

The single nanoindentation test was carried out in load-control mode using a three-sided pyramid Berkovich tip with a maximum load of $F_{max} = 50$ mN at constant loading and an unloading rate of 100 mN/min with 10 seconds dwell at maximum load. The measurements were conducted in a 12×12 indentations grid with 20 μm space between each indentation. The 20 μm distance between the indentations prevents the mutual influence of neighbouring indentations on their mechanical properties. The presented measurement procedure allows covering a surface of 220 μm × 220 μm with 144 indentations. Each indentation was analysed following the Oliver and Pharr protocol. The maps of hardness (HV_{IT}), elastic modulus (E_{IT}), and elastic energy ratio (W_{elast}/W_{total}) were prepared in the same manner for all investigated materials.

SEM/EDS and Mössbauer spectroscopy analysis performed for all manufactured alloys show the complex microstructure of the samples. This fact was also observed in the images obtained with the use of a polarised optical microscope [Figures 7(a), 8(a), 9(a), and 10(a)]. Due to the different brightness regions visible in Figures 7(a), 8(a), 9(a), and 10(a), the two phases were denoted by the authors as phase A (bright regions) and phase B (dark regions). From SEM/EDS microstructure investigations, it was shown that bright regions were
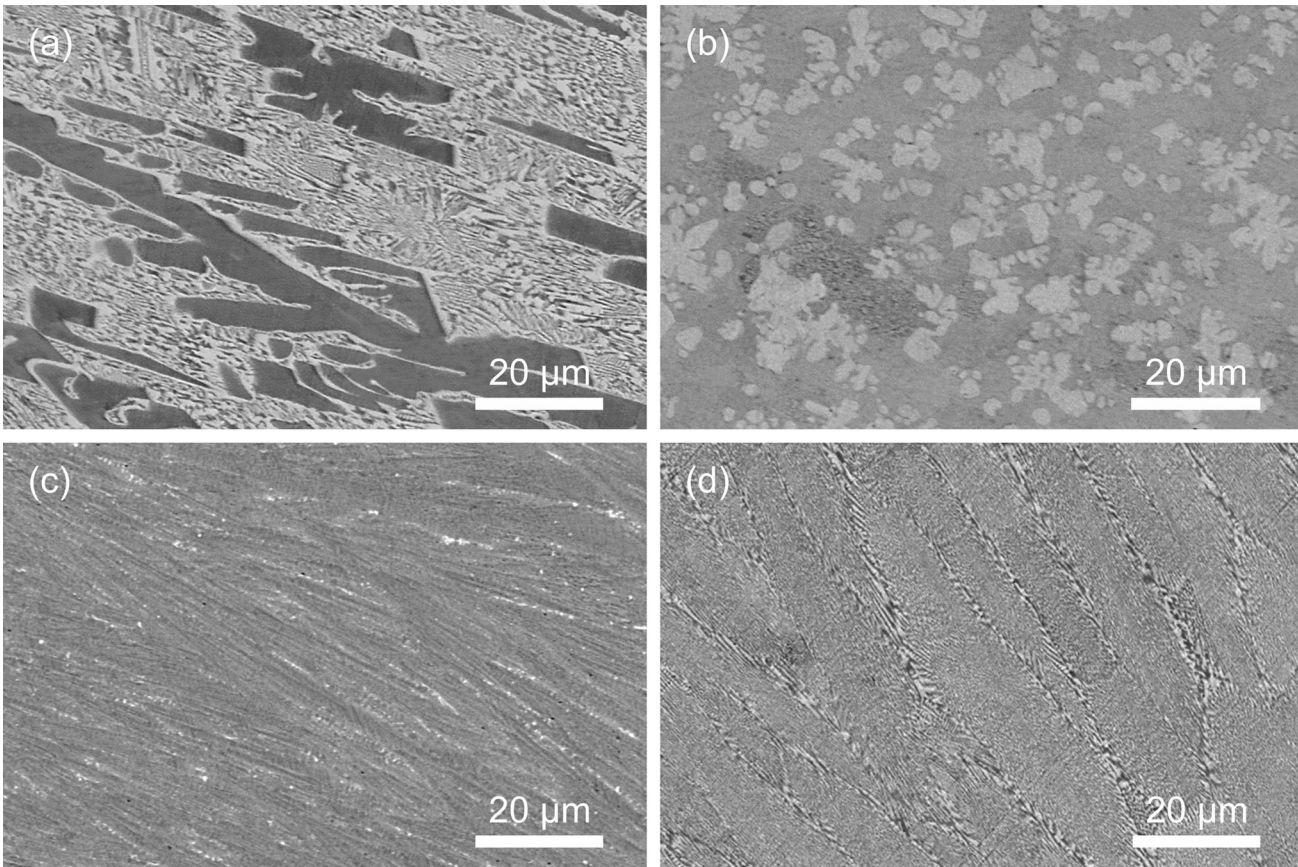
Fig. 5—SEM images obtained with the BSE detector from the central region of the cross-section of the as-cast $Fe_{79}B_{20}Cu_1$ (*a*), $Fe_{79}B_{16}Ti_4Cu_1$ (*b*), $Fe_{79}B_{16}Mo_4Cu_1$ (*c*) and $Fe_{79}B_{16}Mn_4Cu_1$ (*d*) rods.

formed mainly by α-Fe nanograins embedded in an amorphous matrix, while dark regions were created by the segregation of Fe_2B grains. It should be noted that the chemical composition of the amorphous matrix changed due to the diffusion of Fe atoms to the α-Fe and Fe_2B phases in the production process. This fact is also responsible for the change in the mechanical properties of the investigated bright and dark regions observed in the tested alloys. Figures 7 through 10 show the distributions of the instrumental hardness (HV_{IT}), Young's modulus (E_{IT}), elastic energy ratio (W_{elast}/W_{total}), and the corresponding $P(HV_{IT})$, $P(E_{IT})$ and $P(W_{elast}/W_{total})$ histograms for the $Fe_{79}B_{20}Cu_1$, $Fe_{79}B_{16}Ti_4Cu_1$, $Fe_{79}B_{16}Mo_4Cu_1$ and $Fe_{79}B_{16}Mn_4Cu_1$ alloys. It is well seen that for all investigated materials, the two-component histograms $P(HV_{IT})$, $P(E_{IT})$, and $P(W_{elast}/W_{total})$ can be easily distinguished. The first component—marked as phase A (blue colour)—belongs to the bright phase, whereas the second, one—marked as phase B (green colour), belongs to the dark phase. Analysis of HV_{IT}, E_{IT}, and W_{elast}/W_{total} shows that the dark region (phase B) is characterised by higher mechanical properties than the bright region (phase A). Moreover, the differences between the same parameters mentioned above for dark and bright regions as well as for the investigated samples were observed. For example, the instrumental hardness for the basic $Fe_{79}B_{20}Cu_1$ alloy equals 1999 HV and 1508 HV for

phase B and phase A, respectively, *i.e.,* 29 pct difference in hardness. The same trend for basic material was also observed for E_{IT} (308 GPa and 287 GPa for phase B and phase A, respectively) and W_{elast}/W_{total} (44.8 and 37.7 pct for phase B and phase A, respectively). Similar behaviour in mechanical parameters was also observed for doped alloys (Table II). The results obtained for the $Fe_{79}B_{20-x}M_xCu_1$ (where $x = 0$ or 4; M = Ti, Mo, Mn) alloys presented in Table II are comparable to the results reported by other authors.[84–86]

The addition of Ti, Mo and Mn to $Fe_{79}B_{20}Cu_1$ alloy leads to an increase of amorphous matrix and a decrease in the crystalline phase. Therefore, the doped materials show lower HV_{IT}, E_{IT}, and W_{elast}/W_{total} for both bright and dark regions, respectively, compared to the $Fe_{79}B_{20}Cu_1$ alloy. Combining the microstructure observation at different magnifications and distribution of mechanical properties, we can state that all investigated materials show mechanical anisotropy, which is related to the directional quenching of the material during the production process.

C. Magnetic Properties

The next step of materials characterisation was to investigate the magnetic properties of $Fe_{79}B_{20-x}M_xCu_1$ (where $x = 0$ or 4; M = Ti, Mo, Mn) alloys in relation to their microstructure. Figure 11 shows an
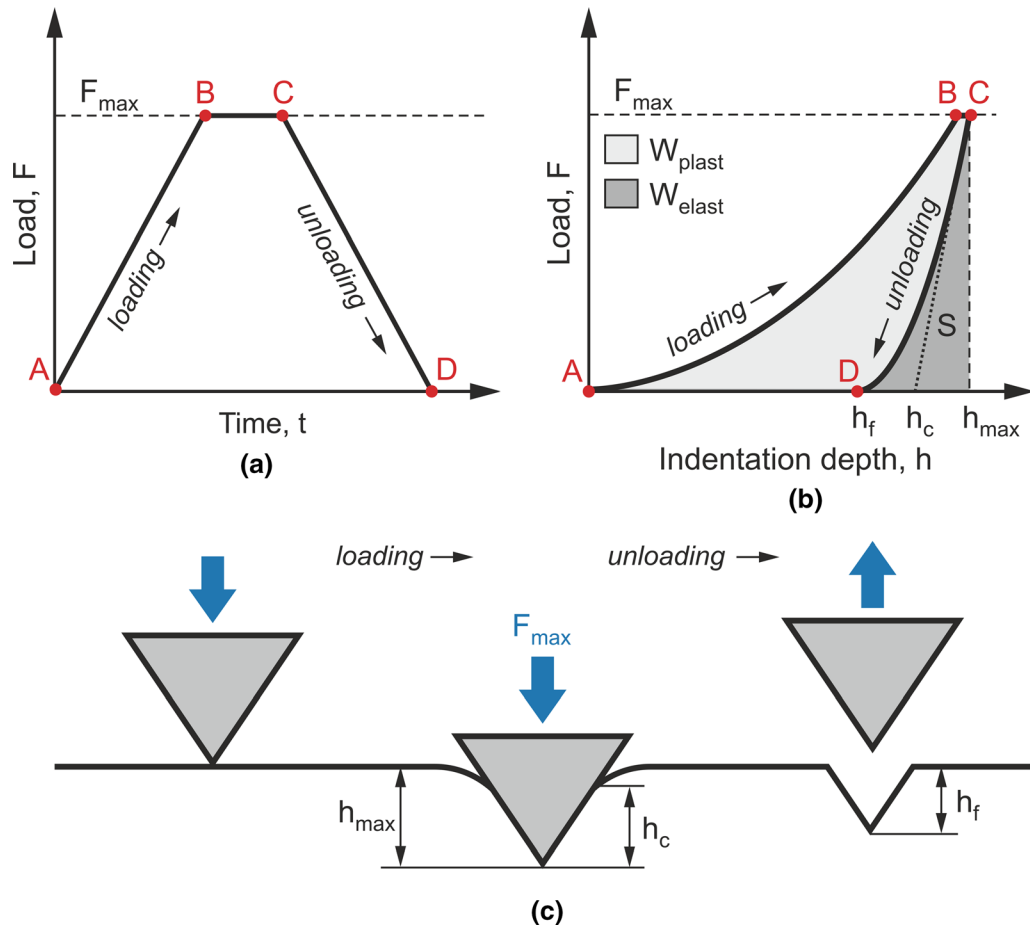
Fig. 6—Schematic representation of the instrumented nanoindentation test. (*a*) Load versus time during load-control indentation: A–B constant loading, B–C dwell time at maximum load, C–D constant unloading; (*b*) typical load-displacement curve during load-control indentation: A–B elastic-plastic loading, B–C dwell time at maximum load, C-D elastic unloading, S—constant stiffness; (*c*) indenter displacement during loading and unloading with marked characteristic displacements: h_{max}—maximum indenter displacement, h_c—contact depth, and h_f—final depth.

example of DC magnetic hysteresis loops $M(H)$ for the $Fe_{79}B_{20}Cu_1$, $Fe_{79}B_{16}Ti_4Cu_1$, $Fe_{79}B_{16}Mo_4Cu_1$ and $Fe_{79}B_{16}Mn_4Cu_1$ alloys recorded at 300 K and in an external magnetic field up to 1200 kA/m. This temperature was chosen for measurement because of the potential application of the tested materials in the electrical engineering industry. The recorded hysteresis loops indicate that all investigated materials belong to a group of soft magnetic materials. The DC coercivity measured for bulk samples in the form of needles was about 5 kA/m for all manufactured materials (Figure 11). The addition of Ti, Mo and Mn elements to the basic $Fe_{79}B_{20}Cu_1$ alloy reveals a slight decrease in magnetic saturation for all doped alloys compared to the $Fe_{79}B_{20}Cu_1$ sample. A slightly lower value of M was observed for the Mo-containing sample. This result is in good agreement with our previous investigations[87,88] performed for amorphous FeMoBCu-type alloys because the addition of Mo leads to a decrease in the Curie point. It is worth noting that the magnetic properties of the investigated materials are comparable because of the similar complex microstructure of these materials and the interaction of Fe atoms with each other.

A similar series of hysteresis loops for all investigated samples was recorded in the temperature range of 50 to 400 K. These loops were used to determine the temperature dependence of the effective magnetic anisotropy using the law of approach to magnetic saturation, which can be expressed by the formula [89–91]:

$$M = M_s\left(1 - \frac{A}{H} - \frac{B}{H^2}\right) + \chi_0 H \qquad [6]$$

where M_s is saturation magnetisation, A is the inhomogeneity parameter, B is the magnetic anisotropy parameter, H is an external magnetic field, and χ_0 is the magnetic susceptibility in a high magnetic field. In the above equation, the term A/H is attributed to the existence of structural defects and non-magnetic inclusions, the term B/H^2 is caused by the magnetocrystalline anisotropy, and the last $\chi_0 H$ term is connected with an increase in the spontaneous magnetisation at high magnetic fields. For manufactured materials, the term $\chi_0 H$ can be neglected as the measurements were performed at temperatures much below the Curie temperature. The term A/H was also not taken into
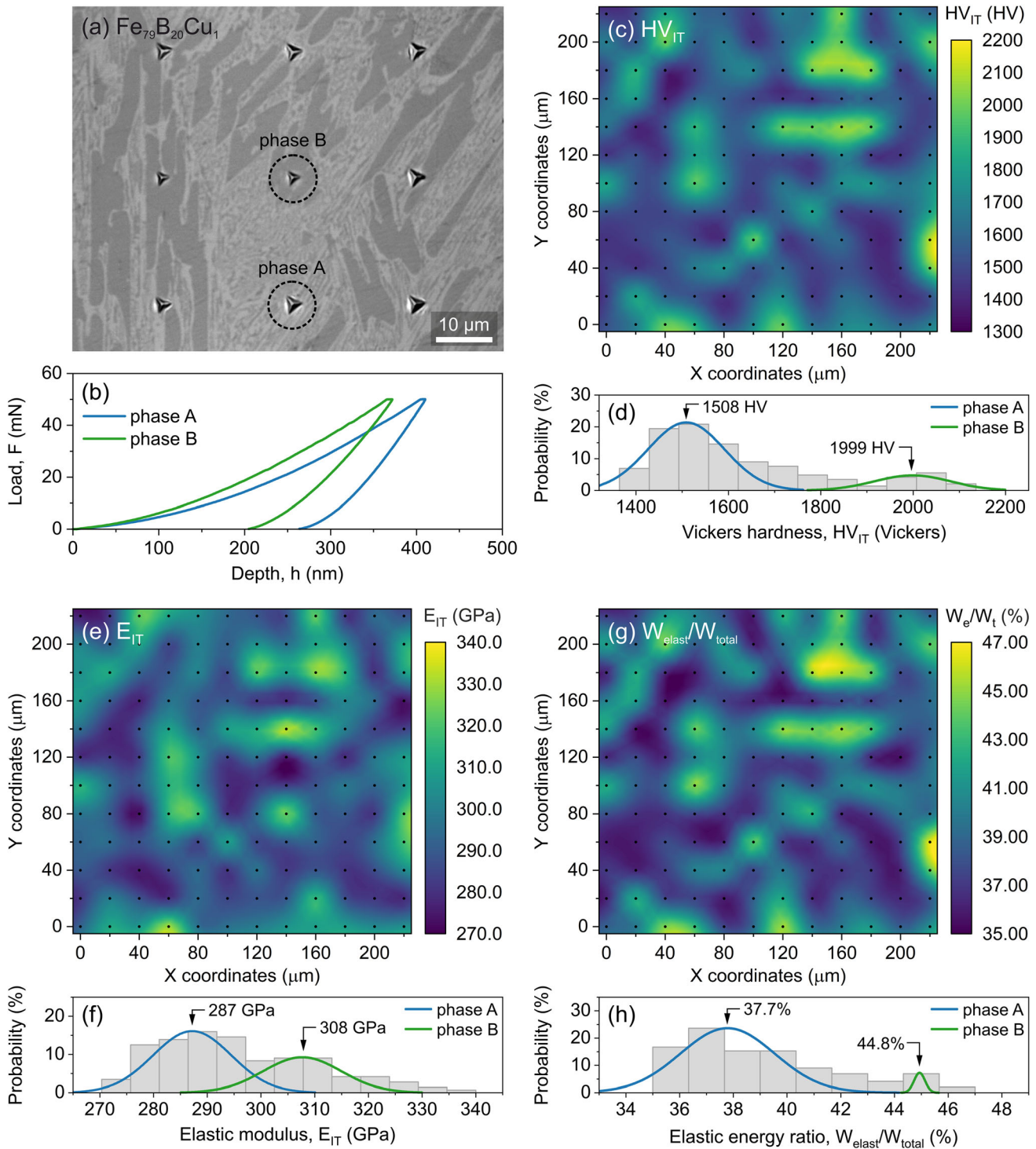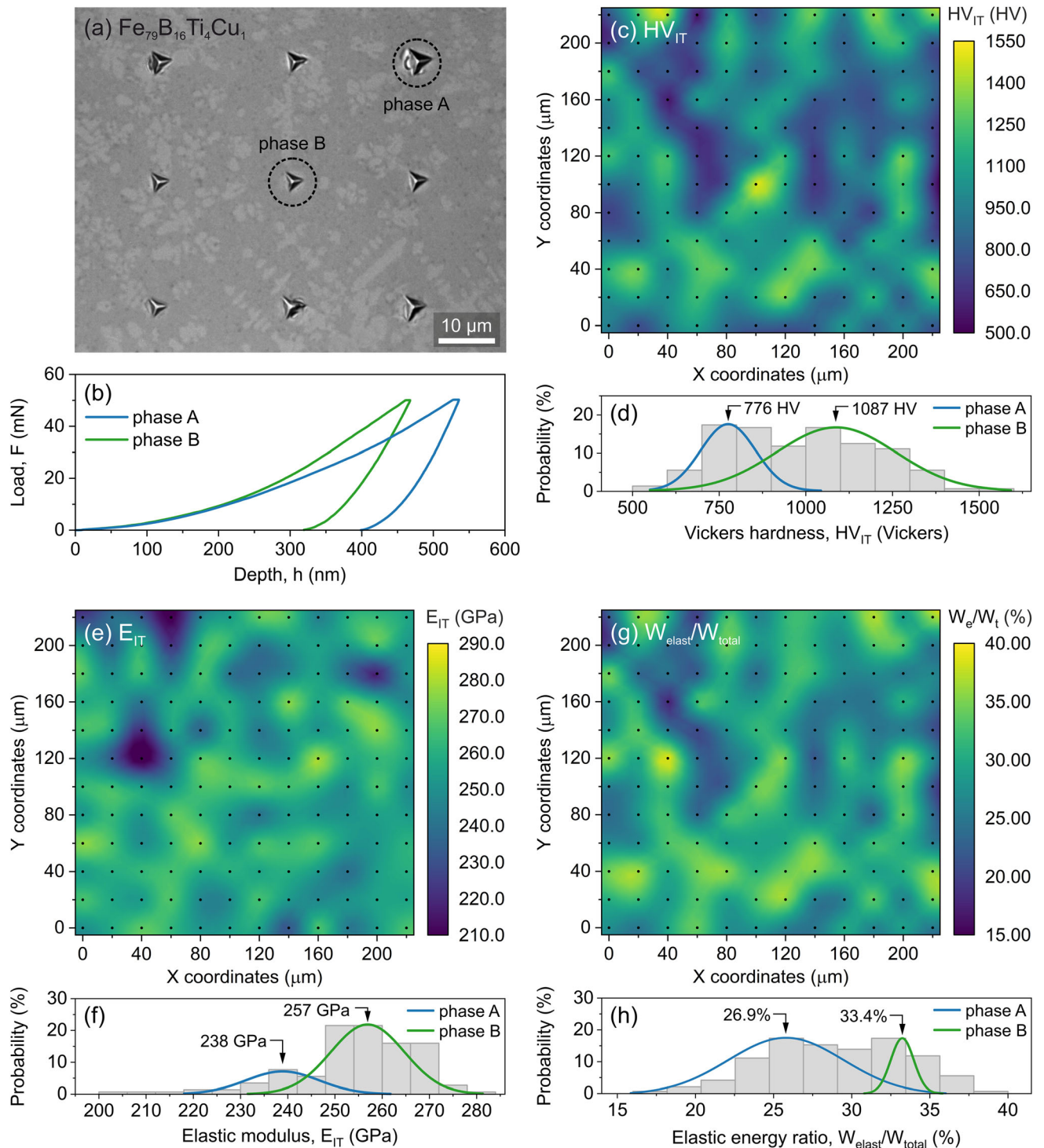
Fig. 7—Surface image (*a*) together with examples of the load-displacement curve (*b*) for the two phases observed in the as-cast $Fe_{79}B_{20}Cu_1$ alloy. The presented maps and corresponding histograms show the distribution of the instrumental hardness HV_{IT} (*c*) to (*d*), Young's modulus E_{IT} (*e*) to (*f*) and elastic energy ratio W_{elast}/W_{tot} (*g*) to (*h*).

consideration because it is valid only for lower magnetic fields.[90,92] Finally, the law of approach to saturation magnetisation for the investigated samples in the high magnetic fields close to magnetic saturation can be expressed by the following formula:
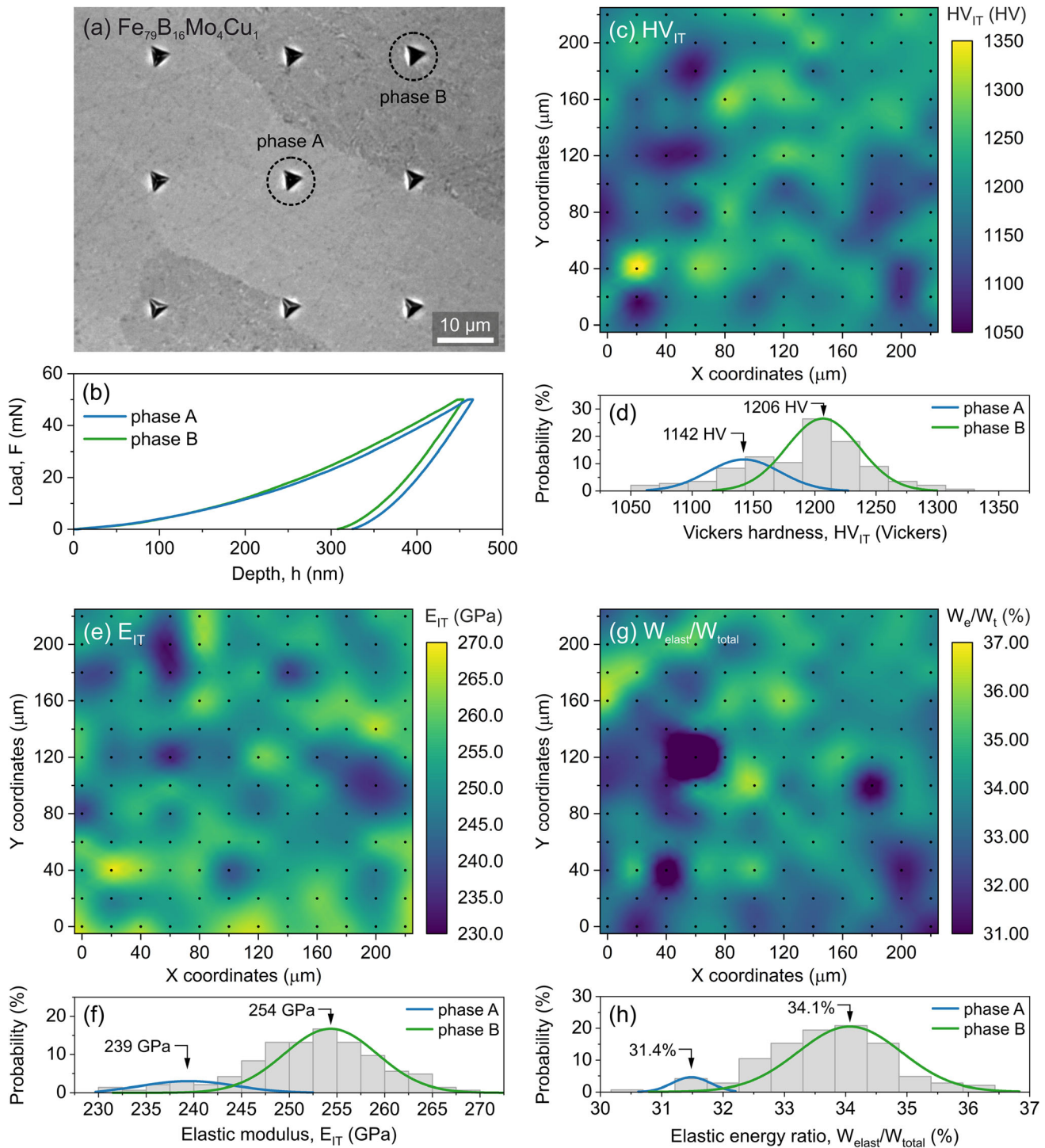
$$M = M_s \left(1 - \frac{B}{H^2}\right) \qquad [7]$$

Fig. 8—Surface image (*a*) together with examples of the load-displacement curve (*b*) for the two phases observed in the as-cast $Fe_{79}B_{16}Ti_4Cu_1$ alloy. The presented maps and corresponding histograms show the distribution of the instrumental hardness HV_{IT} (*c*) to (*d*), Young's modulus E_{IT} (*e*) to (*f*) and elastic energy ratio W_{elast}/W_{tot} (*g*) to (*h*).

High field magnetisation as a function of H^{-2} for the as-cast $Fe_{79}B_{20}Cu_1$, $Fe_{79}B_{16}Ti_4Cu_1$, $Fe_{79}B_{16}Mo_4Cu_1$ and $Fe_{79}B_{16}Mn_4Cu_1$ materials for indicated temperatures is presented in Figure 12 (left column). The linear dependence of high field magnetic magnetisation versus H^{-2} [Figure 12 (left column)] for all materials is evident. This

behaviour shows that the magnetisation is well fitted by the Eq. [7] for magnetic field higher than 1000 kA/m for the $Fe_{79}B_{20}Cu_1$ alloy, 775 kA/m for the $Fe_{79}B_{16}Ti_4Cu_1$ alloy, 970 kA/m for the $Fe_{79}B_{16}Mo_4Cu_1$ alloy and 990 kA/m for the $Fe_{79}B_{16}Mn_4Cu_1$ alloy (Figure 12, left and right column). Taking into account the values of the
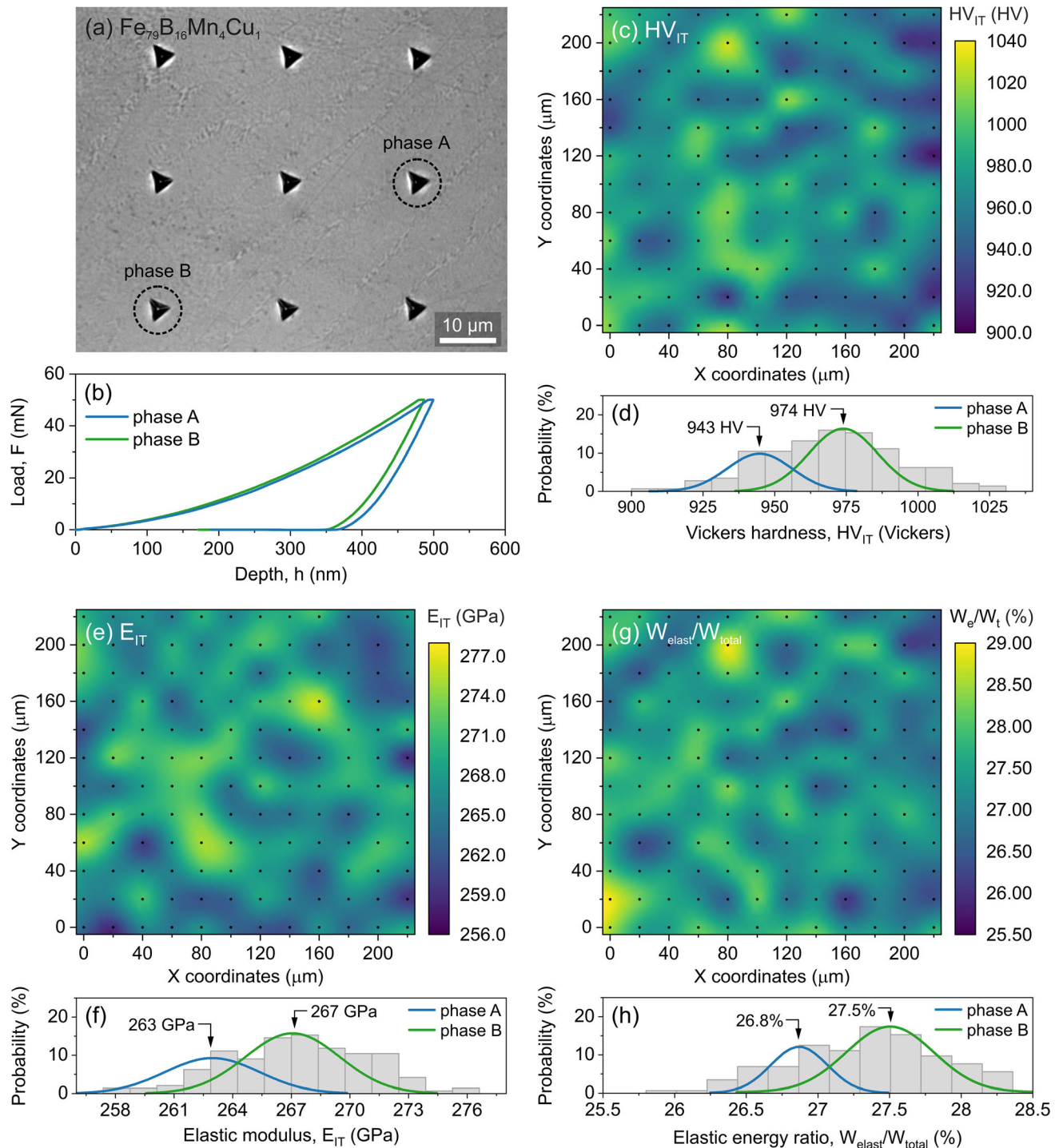
Fig. 9—Surface image (*a*) together with examples of the load-displacement curve (*b*) for the two phases observed in the as-cast $Fe_{79}B_{16}Mo_4Cu_1$ alloy. The presented maps and corresponding histograms show the distribution of the instrumental hardness HV_{IT} (*c*) to (*d*), Young's modulus E_{IT} (*e*) to (*f*) and elastic energy ratio W_{elast}/W_{tot} (*g*) to (*h*).

magnetic field listed above, the recorded points of $M(H)$, in the temperature range 50 to 400 K with the step of 50 K, together with the corresponding fits for all investigated materials, are presented in Figure 12 (right column). The results presented in Figure 12 show a pronounced relationship between the microstructure of the investigated alloys and their soft magnetic

properties. The sample of the $Fe_{79}B_{20}Cu_1$ alloy with 60 pct of the crystalline α-Fe/Fe_2B phases exhibits at room temperature the highest magnetic saturation of 175.6 A·m²/kg, whereas the Mo-containing sample with 23 pct nanocrystalline phase shows the lowest magnetic saturation of 161.3 A·m²/kg at the same condition. The magnetic saturation of the $Fe_{79}B_{16}Ti_4Cu_1$ and

Fig. 10—Surface image (*a*) together with examples of the load-displacement curve (*b*) for the two phases observed in the as-cast $Fe_{79}B_{16}Mn_4Cu_1$ alloy. The presented maps and corresponding histograms show the distribution of the instrumental hardness HV_{IT} (*c*) to (*d*), Young's modulus E_{IT} (*e*) to (*f*) and elastic energy ratio W_{elast}/W_{tot} (*g*) to (*h*).

$Fe_{79}B_{16}Mn_4Cu_1$ alloys at 300 K is equal to 174.7 and 167.9 $A \cdot m^2/kg$, respectively. It is worth noticing that the estimated values of M_s calculated at various temperatures presented in this paper are shown in Figure 13(a) and are comparable to other data reported for nanocrystalline Fe-based alloys[12,93,94] and commercial soft

magnetic FINEMET-[11,95] or HITPERM-type alloys.[96]

The law of approach to magnetic saturation also allows estimating the magnetic anisotropy parameter *B*, which is related to the microstructure of the investigated materials. For Fe-based nanocrystalline alloys, the

Table II. Mechanical Parameters for the $Fe_{79}B_{20}Cu_1$, $Fe_{79}B_{16}Ti_4Cu_1$, $Fe_{79}B_{16}Mo_4Cu_1$ and $Fe_{79}B_{16}Mn_4Cu_1$ Alloys for Phase A (Bright Area) and Phase B (Dark Area) Obtained From Numerical Analysis of $P(HV_{IT})$, $P(E_{IT})$ and $P(W_{elast}/W_{total})$ Distributions

Sample	HV_{IT} (HV)		E_{IT} (GPa)		W_{elast}/W_{total} (Pct)	
	Phase A	Phase B	Phase A	Phase B	Phase A	Phase B
$Fe_{79}B_{20}Cu_1$	1508 ± 20	1999 ± 100	287 ± 3	308 ± 5	37.7 ± 1.2	44.8 ± 0.3
$Fe_{79}B_{16}Ti_4Cu_1$	780 ± 10	1090 ± 40	238 ± 18	257 ± 6	26.9 ± 2.5	33.4 ± 0.2
$Fe_{79}B_{16}Mo_4Cu_1$	1140 ± 30	1210 ± 10	239 ± 6	254 ± 1	31.4 ± 0.2	34.1 ± 0.5
$Fe_{79}B_{16}Mn_4Cu_1$	940 ± 10	970 ± 10	263 ± 15	267 ± 9	26.8 ± 0.1	27.5 ± 0.2
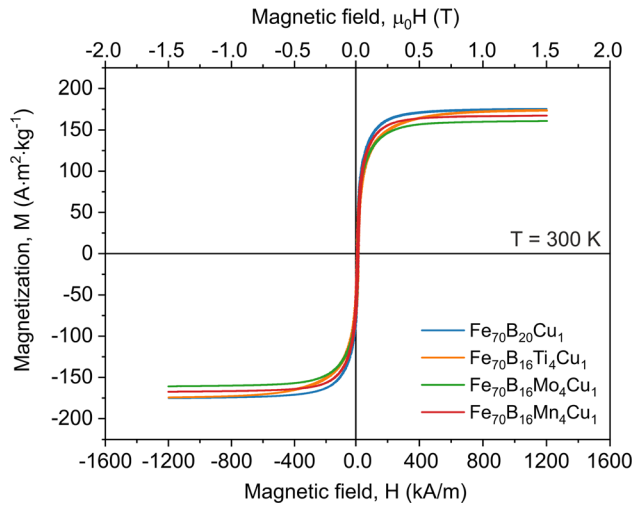
Fig. 11—DC magnetic hysteresis loops for the $Fe_{79}B_{20}Cu_1$ (a), $Fe_{79}B_{16}Ti_4Cu_1$ (b), $Fe_{79}B_{16}Mo_4Cu_1$ (c) and $Fe_{79}B_{16}Mn_4Cu_1$ (d) alloys recorded at 300 K for maximum external magnetic field of 1200 kA/m.

coefficient B is expressed with the following equation[97,98]:

$$B = \frac{4}{15} K_{eff}^2 / M_s^2 \qquad [8]$$

where K_{eff} is the effective anisotropy constant, M_s is the saturation magnetisation, and B is the magnetocrystalline anisotropy parameter.

According to Eq. [8], the effective anisotropy constant K_{eff} was calculated from:

$$K_{eff} = \frac{1}{2} M_s \sqrt{15B} \qquad [9]$$

Figure 13 shows the temperature dependence of saturation magnetisation and the corresponding anisotropy constant, calculated from Eq. [9], for the manufactured $Fe_{79}B_{20}Cu_1$, $Fe_{79}B_{16}Ti_4Cu_1$, $Fe_{79}B_{16}Mo_4Cu_1$ and $Fe_{79}B_{16}Mn_4Cu_1$ alloys. It is well seen that $M_s(T)$ dependences [Figure 13(a)] are typical for ferromagnetic materials. Investigations of the effective anisotropy constant for the $Fe_{79}B_{20}Cu_1$ and $Fe_{79}B_{16}Ti_4Cu_1$ alloys exhibit a significant decrease in K_{eff} with increasing temperature. In the case of the $Fe_{79}B_{20}Cu_1$ and $Fe_{79}B_{16}Ti_4Cu_1$ samples, the anisotropy constant

decreased from $3.82 \cdot 10^5$ J/m^3 at 50 K to $2.74 \cdot 10^5$ J/m^3 at 400 K, and from $5.05 \cdot 10^5$ J/m^3 at 50 K to $3.83 \cdot 10^5$ J/m^3 at 400 K, respectively. Even though M_s for the materials mentioned above are close in the temperature range 50 – 400 K, the values of K_{eff} for the $Fe_{79}B_{20}Cu_1$ and $Fe_{79}B_{16}Ti_4Cu_1$ alloys differ by about 50 pct [Figure 13(b)] at the same temperature range. In contrast to the $Fe_{79}B_{20}Cu_1$ and $Fe_{79}B_{16}Ti_4Cu_1$ alloys, the temperature dependence of magnetocrystalline anisotropy for the $Fe_{79}B_{16}Mo_4Cu_1$ and $Fe_{79}B_{16}Mn_4Cu_1$ alloys is not as evident. The values of K_{eff} for Mo- and Mn-containing samples estimated at room temperature are equal to $2.79 \cdot 10^5$ and $2.70 \cdot 10^5$ J/m^3, respectively. It should be noted that at room temperature, the $Fe_{79}B_{16}Mn_4Cu_1$ alloy shows the lowest value of magnetocrystalline anisotropy and the lowest differences in mechanical properties between individual phases recognised in this material.

On the basis of the obtained results, the strong correlation between mechanical and magnetic properties is visible for all investigated materials. Figure 14 shows the relation between the effective magnetocrystalline anisotropy constant and the relative differences between the hardness $((HV_{ITB} - HV_{ITA})/HV_{ITB})$, and the elastic modulus $[(E_{ITB} - E_{ITA})/E_{ITB}]$ of the observed phases (phase A and phase B) in the $Fe_{79}B_{20-x}M_xCu_1$ (where $x = 0$ or 4; M = Ti, Mo, Mn) alloys. It is seen that with increasing K_{eff}, a similar increasing tendency in terms of $(HV_{ITB} - HV_{ITA})/HV_{ITB}$ and $(E_{ITB} - E_{ITA})/E_{ITB}$ is observed. The Ti-containing sample, characterised by globular dendrites [Figure 5(b)] and lack of paramagnetic ordering [Figure 2(b, f)] shows the highest magnetic and mechanical anisotropy, whereas the $Fe_{79}B_{16}Mn_4Cu_1$ alloy with the most refined microstructure [Figure 5(d)] presents the lowest values of K_{eff}, $(HV_{ITB} - HV_{ITA})/HV_{ITB}$ and $(E_{ITB} - E_{ITA})/E_{ITB}$.

IV. CONCLUSIONS

The novel, low cost, nanocrystalline bulk $Fe_{79}B_{20}Cu_1$, $Fe_{79}B_{16}Ti_4Cu_1$, $Fe_{79}B_{16}Mo_4Cu_1$ and $Fe_{79}B_{16}Mn_4Cu_1$ alloys were manufactured directly in a rapid cooling process in the form of rods of 3 mm in diameter. Microstructure investigations carried out using TEM and Mössbauer Spectroscopy confirmed the presence of amorphous and nanocrystalline α-Fe and Fe_2B phases in all manufactured materials. The addition of alloying
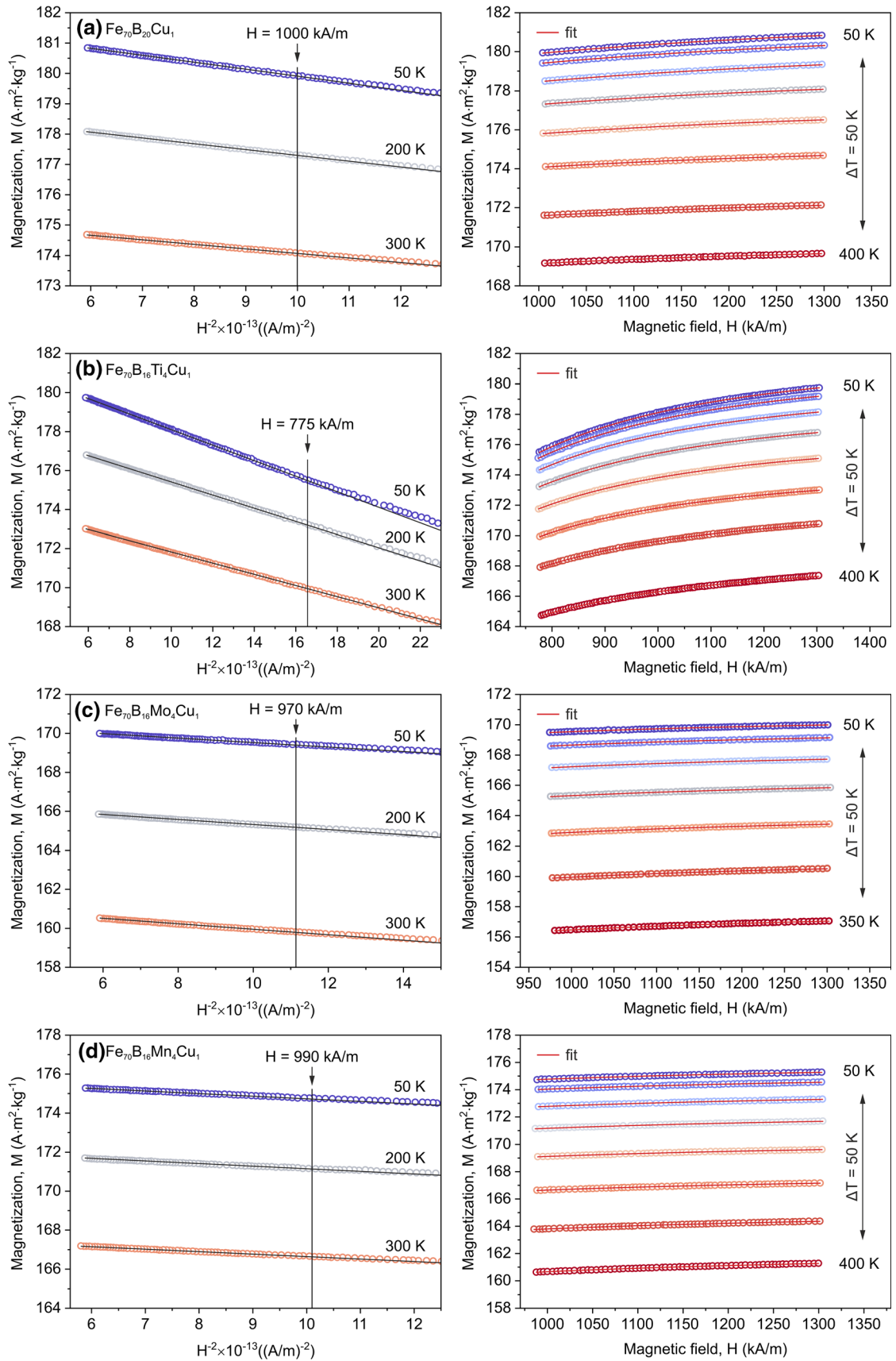
Fig. 12—Magnetisation M as a function of H^{-2} (left column) and H (right column) at various temperatures for the as-cast $Fe_{79}B_{20}Cu_1$ (*a*), $Fe_{79}B_{16}Ti_4Cu_1$ (*b*), $Fe_{79}B_{16}Mo_4Cu_1$ (*c*) and $Fe_{79}B_{16}Mn_4Cu_1$ (*d*) alloys.
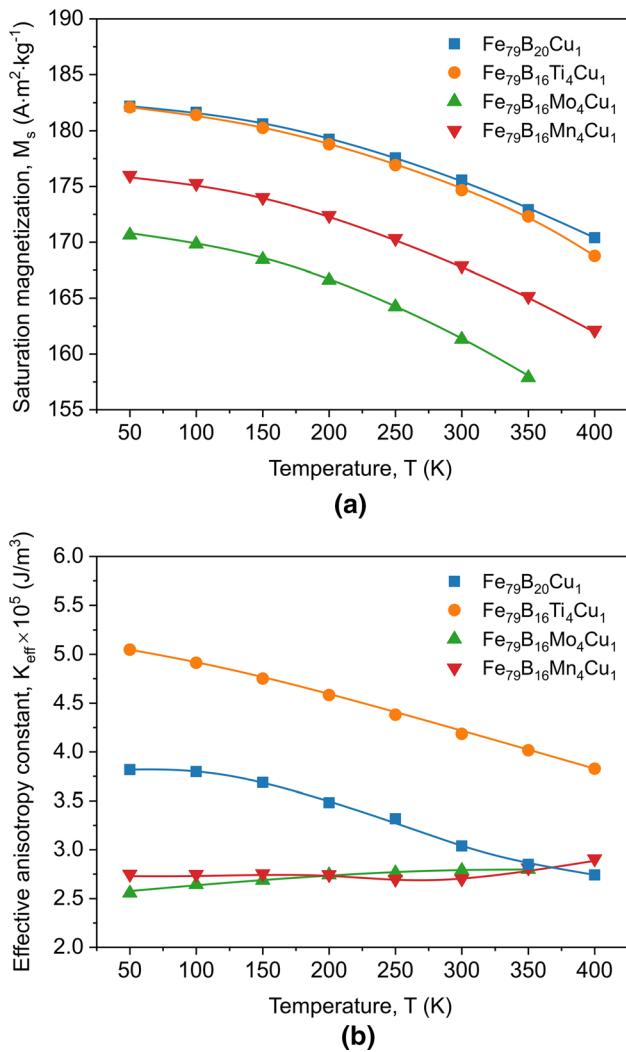
(a)

(b)

Fig. 13—Saturation magnetisation M_s (*a*) and effective anisotropy constant K_{eff} (*b*) versus temperature obtained from numerical analysis of the initial magnetisation curve for the as-cast $Fe_{79}B_{20}Cu_1$ (*a*), $Fe_{79}B_{16}Ti_4Cu_1$ (*b*), $Fe_{79}B_{16}Mo_4Cu_1$ (*c*) and $Fe_{79}B_{16}Mn_4Cu_1$ (*d*) alloys.

Fig. 14—3D plot showing the relationship between magnetocrystalline anisotropy K_{eff} and mechanical anisotropy measured as percentage differences between both hardness $(HV_{ITB} - HV_{ITA})/HV_{ITB}$ and elastic modulus $(E_{ITB} - E_{ITA})/E_{ITB}$ of the two phases (bright—phase A and dark—phase B) observed in the $Fe_{79}B_{20}Cu_1$, $Fe_{79}B_{16}Ti_4Cu_1$, $Fe_{79}B_{16}Mo_4Cu_1$ and $Fe_{79}B_{16}Mn_4Cu_1$ alloys.

elements increases the amorphous matrix and decreases the content of the nanocrystalline α-Fe + Fe_2B phase. SEM/BSE observations on a microscale level showed that the manufactured alloys contain dark and bright regions differing in chemical composition. The size and dispersion of these regions change with alloying additions.

The mechanical properties such as hardness, Young's modulus, and the elastic energy ratio for the regions visible in manufactured alloys were investigated. The nanoindentation tests performed on a 12×12 matrix allowed to estimate the mechanical parameters of each region in the analysed materials. It was shown that the amorphous rich regions (phase A) are characterised by lower values of hardness and elastic modulus than nanocrystalline-rich areas (phase B). The highest values
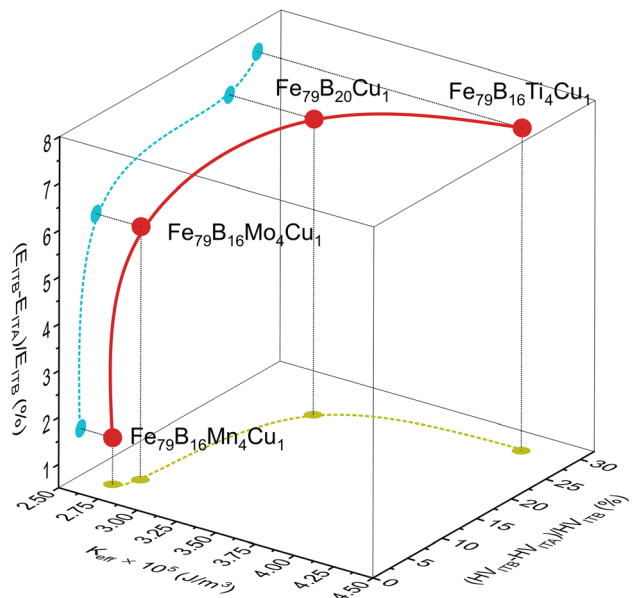
of HV_{IT}, E_{IT}, and W_{elast}/W_{total} for both phase A and phase B were calculated for the $Fe_{79}B_{20}Cu_1$ alloy. The addition of Ti, Mo, and Mn leads to a decrease in the mechanical properties in the as-cast materials.

Thermomagnetic characteristics recorded in a wide range of temperature and magnetic fields were used to characterise the soft magnetic properties of the manufactured materials. It was shown that the alloying elements used in the production process do not change the magnetic properties significantly. The magnetisation estimated from the hysteresis loops recorded at room temperature for all samples is about 170 A·m²/kg. To determine the temperature dependence of the saturation magnetisation and the effective magnetic anisotropy, the law of approach to magnetic saturation was applied considering the high field magnetisation data. The highest values of the effective anisotropy constant K_{eff} in the temperature range 50 - 400 K were estimated for the $Fe_{79}B_{16}Ti_4Cu_1$ alloy, which is also connected with the lack of paramagnetic ordering within the amorphous matrix indicated in the Mössbauer studies.

The investigations performed for the $Fe_{79}B_{20-x}M_xCu_1$ (where $x = 0$ or 4; M = Ti, Mo, Mn) alloys suggest a strong correlation between mechanical and magnetic properties for all investigated materials. The addition of the studied alloying elements to the $Fe_{79}B_{20}Cu_1$ alloy results in significant microstructural changes, which influence the physical properties of Ti-, Mo- and Mn-containing samples.

CONFLICT OF INTEREST

The authors declare that they have no conflicts of interest.

OPEN ACCESS

REFERENCES

1. W. Klement, R.H. Willens, and P. Duwez: *Nature*, 1960, vol. 187, pp. 869–70.
2. A. Inoue, T. Zhang, T. Itoi, and A. Takeuchi: *Met. Trans. JIM*, 1997, vol. 38, pp. 359–62.
3. M. Brouha and J. van der Borst: *J. Appl. Phys.*, 1979, vol. 50, p. 7594.
4. Y. Geng, Y. Wang, J. Qiang, G. Zhang, C. Dong, and P. Häussler: *J. Non-Cryst. Solids*, 2016, vol. 432, pp. 453–58.
5. L.L. Pang, A. Inoue, E.N. Zanaeva, F. Wang, A.I. Bazlov, Y. Han, F.L. Kong, S.L. Zhu, and R.B. Shull: *J. Alloy Compd.*, 2019, vol. 785, pp. 25–37.
6. X.B. Zhai, Y.G. Wang, L. Zhu, H. Zheng, Y.D. Dai, J.K. Chen, and F.M. Pan: *J. Magn. Magn. Mater.*, 2019, vol. 480, pp. 47–52.
7. A. Inoue and A. Takeuchi: *Acta Mater.*, 2011, vol. 59, pp. 2243–67.
8. M. Miller and P. Liaw: *Bulk Metallic Glasses: An Overview*, Springer, New York, 2007.
9. J. Cheney and K. Vecchio: *Mater. Sci. Eng. A*, 2008, vol. 492, pp. 230–35.
10. M. Hagiwara and A. Inoue: *Rapidly Solidified Alloys*, CRC Press, Boca Raton, 1993, pp. 153–70.
11. A. Inoue, B.L. Shen, and C.T. Chang: *Intermetallics*, 2006, vol. 14, pp. 936–44.
12. A. Inoue and X.M. Wang: *Acta Mater.*, 2000, vol. 48, pp. 1383–95.
13. S. Guo and Y. Shen: *Trans. Met. Soc. China*, 2011, vol. 21, pp. 2433–37.
14. X.M. Huang, C.T. Chang, Z.Y. Chang, X.D. Wang, Q.P. Cao, B.L. Shen, A. Inoue, and J.Z. Jiang: *J. Alloy Compd.*, 2008, vol. 460, pp. 708–13.
15. V. Ponnambalam, S.J. Poon, and G.J. Shiflet: *J. Mater. Res.*, 2004, vol. 19, pp. 1320–23.
16. A. Inoue and B. Shen: *Mater. Trans.*, 2002, vol. 43, pp. 766–69.
17. A. Grabias, D. Oleszak, J. Latuch, T. Kulik, and M. Kopcewicz: *J. Magn. Magn. Mater.*, 2004, vols. 272–276, pp. E1141–43.
18. J. Zhang, C. Chang, A. Wang, and B. Shen: *J. Non-Cryst. Solids*, 2012, vol. 358, pp. 1443–46.
19. M.E. McHenry, F. Johnson, H. Okumura, T. Ohkubo, V.R.V. Ramanan, and D.E. Laughlin: *Scr. Mater.*, 2003, vol. 48, pp. 881–7.
20. J. Torrens-Serra, I. Peral, J. Rodriguez-Viejo, and M.T. Clavaguera-Mora: *J. Non-Cryst. Solids*, 2012, vol. 358, pp. 107–13.
21. M. Sorescu, T. Xu, and S. Herchko: *J. Magn. Magn. Mater.*, 2011, vol. 323, pp. 2859–65.
22. M.E. McHenry, M.A. Willard, and D.E. Laughlin: *Prog. Mater Sci.*, 1999, vol. 44, pp. 291–433.
23. M. Miglierini, M. Kopcewicz, B. Idzikowski, Z.E. Horváth, A. Grabias, I. Škovánek, P. Duźewski, and Cs.S. Daróczi: *Journal of Applied Physics*, 1999, vol. 85, pp. 1014–25.
24. J. Swierczek: *J. Alloy. Compd.*, 2014, vol. 615, pp. 255–262.
25. S. Lesz, D. Szewieczek, and J. Tyrlik-Held: *Arch. Mater. Sci. Eng.*, 2008, vol. 29 (2), pp. 73–80.
26. D. Szewieczek, J. Tyrlik-Held, and S. Lesz: *J. Achiev. Mater. Manuf. Eng.*, 2007, vol. 24 (2), pp. 87–90.
27. I. Skorvánek, P. Svec, J-.M. Grenèche, J. Kovác, J. Marcin, and R. Gerling: *J. Phys. Condens. Matter*, 2002, vol. 14, pp. 4717–36.
28. J. Qiao, H. Jia, and P.K. Liaw: *Mater. Sci. Eng. R. Rep.*, 2016, vol. 100, pp. 1–69.
29. A. Inoue: *Mater. Sci. Eng. A*, 2001, vols. 304–306, pp. 1–10.
30. P. Rezaei-Shahreza, A. Seifoddini, and S. Hasani: *J. Alloy Compd.*, 2018, vol. 738, pp. 197–205.
31. C.C. Hays, C.P. Kim, and W.L. Johnson: *Phys. Rev. Lett.*, 2000, vol. 84, pp. 2901–04.
32. X. Wu, W. Zhao, and L. Meng: *Trans. Nonferrous Met. Soc. China*, 2009, vol. 19, pp. 72–77.
33. F. Szuecs, CP. Kim, and W.L. Johnson: *Acta Mater.*, 2001, vol. 49, pp. 1507–13.
34. J. Eckert, J. Das, S. Pauly, and C. Duhamel: *J. Mater. Res.*, 2007, vol. 22, pp. 285–301.
35. S.F. Guo, L. Liu, N. Li, and Y. Li: *Scr. Mater.*, 2010, vol. 62, pp. 329–32.
36. S. Guo and C. Su: *Mater. Sci. Eng. A*, 2017, vol. 707, pp. 44–50.
37. J.M. Park, D.H. Kim, K.B. Kim, N. Mattern, and J. Eckert: *J. Mater. Res.*, 2011, vol. 26, pp. 365–71.
38. C. Yang, J. Zhang, H. Huang, Q. Song, and F. Liu: *Physica B*, 2015, vol. 476, pp. 132–36.
39. R. Li, S. Pang, M. Stoica, J.M. Park, U. Kühn, T. Zhang, and J. Eckert: *J. Alloy Compd.*, 2010, vol. 504, pp. S472–75.
40. H. Huang, C. Yang, Q. Song, K. Ye, and F. Liu: *J. Appl. Phys.*, 2016, https://doi.org/10.1063/1.4959801.
41. J.M. Park, D.H. Kim, K.B. Kim, M.H. Lee, W.T. Kim, and J. Eckert: *J. Mater. Res.*, 2008, vol. 23, pp. 2003–08.
42. H.Y. Jung, M. Stoica, S. Yi, D.H. Kim, and J. Eckert: *Intermetallics*, 2016, vol. 69, pp. 54–61.
43. F.F. Wu, K.C. Chan, SS. Jiang, S.H. Chen, and G. Wang: *Sci. Rep.*, 2014, vol. 4, pp. 1–6.
44. Y.H. Zhu, S.F. Ge, H. Li, A.M. Wang, H.F. Zhang, and Z.W. Zhu: *J. Alloys Compds.*, 2021, https://doi.org/10.1016/j.jallcom.2020.158149.
45. Z.Y. Zhang, Y. Wu, J. Zhou, H. Wang, X.J. Liu, and Z.P. Lu: *Scr. Mater.*, 2013, vol. 69, pp. 73–76.
46. C. Jeon, C.P. Kim, S.H. Joo, H.S. Kim, and S. Lee: *Acta Mater.*, 2013, vol. 61, pp. 3012–26.
47. L. Zhang, R.L. Narayan, H.M. Fu, U. Ramamurty, W.R. Li, Y.D. Li, and H.F. Zhang: *Acta Mater.*, 2019, vol. 168, pp. 24–36.
48. X.L. Zhang, G. Chen, and T. Bauer: *Intermetallics*, 2012, vol. 29, pp. 56–60.
49. J.L. Soubeyroux, S. Puech, P. Donnadieu, and J.J. Blandin: *J. Alloy Compd.*, 2007, vols. 434–435, pp. 84–87.
50. J.I. Lee, W.H. Ryu, K.N. Yoon, and E.S. Park: *J. Alloys Compds.*, 2021, vol. 879, p. 160417.
51. D. dan Liang, X. Shun Wei, C. Tao Chang, J. Wei Li, X. Min Wang, and J. Shen: *J. Alloys Compds.*, 2018, vol. 731, pp. 1146–50.
52. M. Li, H. Guan, S. Yang, X. Ma, and Q. Li: *Mater. Sci. Eng. A*, 2021, https://doi.org/10.1016/j.msea.2020.140542.
53. B. Shen, H. Men, and A. Inoue: *Appl. Phys. Lett.*, 2006, https://doi.org/10.1063/1.2348737.
54. Y.C. Liao, S.M. Song, T.H. Li, P.H. Tsai, C.Y. Chen, J.S.C. Jang, J.P. Chu, and C.M. Tseng: *Mater. Chem. Phys.*, 2020, vol. 241, p. 122281.
55. D.C. Hofmann, J.Y. Suh, A. Wiest, G. Duan, M.L. Lind, M.D. Demetriou, and W.L. Johnson: *Nature*, 2008, vol. 451, pp. 1085–89.
56. G. Zhang, Q. Wang, C. Yuan, W. Yang, J. Zhou, L. Xue, F. Hu, B. Sun, and B. Shen: *J. Alloy Compd.*, 2018, vol. 737, pp. 815–20.
57. K. Kosiba and S. Pauly: *Sci. Rep.*, 2017, vol. 7, p. 2151.

58. X.F. Liu, Y. Chen, M.Q. Jiang, P.K. Liaw, and L.H. Dai: *Mater. Sci. Eng. A*, 2017, vol. 680, pp. 121–29.
59. S. González, I.A. Figueroa, H. Zhao, H.A. Davies, I. Todd, and P. Adeva: *Intermetallics*, 2009, vol. 17, pp. 968–71.
60. M. Hasiak, K. Sobczyk, J. Zbroszczyk, W. Ciurzynska, J. Olszewski, M. Nabialek, J. Kaleta, J. Swierczek, and A. Lukiewska: *IEEE Trans. Magn.*, 2008, vol. 44, pp. 3879–82.
61. J. Zbroszczyk, J. Olszewski, W. Ciurzyńska, M. Nabiałek, P. Pawlik, M. Hasiak, A. Łukiewska, and K. Perduta: *J. Magn. Magn. Mater.*, 2006, vol. 304, pp. 724–26.
62. G.R. Khanolkar, M.B. Rauls, J.P. Kelly, O.A. Graeve, A.M. Hodge, and V. Eliasson: *Sci. Rep.*, 2016, vol. 6, pp. 1–9.
63. M. Chen: *NPG Asia Mater.*, 2011, vol. 3, pp. 82–90.
64. Y. Naitoh, T. Bitoh, T. Hatanai, A. Makino, A. Inoue, and T. Masumoto: *Nanostruct. Mater.*, 1997, vol. 8, pp. 987–95.
65. A. Makino, T. Hatanai, A. Inoue, and T. Masumoto: *Mater. Sci. Eng. A*, 1997, vols. 226–228, pp. 594–602.
66. A. Inoue, F.L. Kong, Q.K. Man, BL. Shen, R.W. Li, and F. Al-Marzouki: *J. Alloy Compd.*, 2015, vol. 615, pp. S2–S8.
67. A. Makino, C. Chang, T. Kubota, and A. Inoue: *J. Alloy Compd.*, 2009, vol. 483, pp. 616–19.
68. T.D. Shen and R.B. Schwarz: *Appl. Phys. Lett.*, 1999, vol. 75, pp. 49–51.
69. A. Inoue: *Acta Mater.*, 2000, vol. 48, pp. 279–306.
70. K. Suzuki, A. Makino, N. Kataoka, A. Inoue, and T. Masumoto: *Mater. Trans. JIM*, 1991, vol. 32, pp. 93–102.
71. D. Mishra, A. Perumal, P. Saravanan, D. Arvindha Babu, and A. Srinivasan: *J. Magn. Magn. Mater.*, 2009, vol. 321, pp. 4097–4102.
72. H. Chiriac and N. Lupu: *J. Magn. Magn. Mater.*, 2000, vols. 215–216, pp. 394–96.
73. H.X. Li, K.B. Kim, and S. Yi: *Scr. Mater.*, 2007, vol. 56, pp. 1035–38.
74. X.H. Lin and W.L. Johnson: *J. Appl. Phys.*, 1995, vol. 78, pp. 6514–19.
75. L. Wang, J. Wang, and M. Sun: *Chem. Phys. Lett.*, 2020, vol. 750, p. 137511.
76. M. Tkaczyk, M. Hasiak, J. Kaleta, and K.I. Dragnevski: *Mater. Today Proc.*, 2020, vol. 33, pp. 1775–80.
77. R.A. Brand: *Nucl. Instrum. Methods Phys. Res. Sect. B*, 1987, vol. 28, pp. 398–416.
78. W.C. Oliver and G.M. Pharr: *J. Mater. Res.*, 2004, vol. 19, pp. 3–20.
79. J. Hesse and A. Rubartsch: *J. Phys. E*, 1974, vol. 7, pp. 526–32.
80. EC. Passamani, J.R.B. Tagarro, C. Larica, and A.A.R. Fernandes: *J. Phys. Condens. Matter*, 2002, vol. 14, pp. 1975–83.
81. K. Sobczyk, J. Świerczek, J. Gondro, J. Zbroszczyk, W.H. Ciurzyńska, J. Olszewski, P. Brągiel, A. Łukiewska, J. Rzącki, and M. NabiaŁek: *J. Magn. Magn. Mater.*, 2012, vol. 324, pp. 540–49.
82. M. Hasiak, M. Miglierini, J. Kaleta, J. Zbroszczyk, and E. Zschech: *J. Magn. Magn. Mater.*, 2008, vol. 320, pp. e783–86.
83. A.I. Taub: *J. Appl. Phys.*, 1984, vol. 55, pp. 1775–77.
84. H.R. Lashgari, Z. Chen, X.Z. Liao, D. Chu, M. Ferry, and S. Li: *Mater. Sci. Eng. A*, 2015, vol. 626, pp. 480–99.
85. E. Dastanpour, M.H. Enayati, A. Masood, and V. Ström: *J. Alloys Compds.*, 2021, vol. 851, p. 156727.
86. H.R. Lashgari, J.M. Cadogan, D. Chu, and S. Li: *Mater. Des.*, 2016, vol. 92, pp. 919–31.
87. M. Hasiak and A. Laszcz: *IEEE Trans. Magn.*, 2018, https://doi.org/10.1109/TMAG.2018.2883026.
88. M. Hasiak, M. Miglierini, M. Łukiewski, A. Łaszcz, and M. Bujdoš: *AIP Adv.*, 2018, vol. 8, pp. 4–9.
89. R. Grössinger: *J. Magn. Magn. Mater.*, 1982, vol. 28, pp. 137–42.
90. S.V. Andreev, M.I. Bartashevich, V.I. Pushkarsky, V.N. Maltsev, L.A. Pamyatnykh, E.N. Tarasov, N.V. Kudrevatykh, and T. Goto: *J. Alloys Compds.*, 1997, vol. 260, pp. 196–200.
91. Y. Melikhov, J. Snyder, C. Lo, P. Matlage, S. Song, K. Dennis, and D. Jiles: *INTERMAG 2006 - IEEE International Magnetics Conference*, 2006.
92. S. Chikazumi: *Physics*, https://doi.org/10.1007/978-3-642-25583-0.
93. K. Suzuki, A. Makino, A. Inoue, and T. Masumoto: *J. Appl. Phys.*, 1993, vol. 74, pp. 3316–22.
94. I. Škorvánek, J. Marcin, J. Turčanová, J. Kováč, and P. Švec: *J. Alloy Compd.*, 2010, vol. 504, pp. S135–38.
95. H. Okumura, D.E. Laughlin, and M.E. McHenry: *J. Magn. Magn. Mater.*, 2003, vol. 267, pp. 347–56.
96. X. Liang, T. Kulik, J. Ferenc, and B. Xu: *J. Magn. Magn. Mater.*, 2007, vol. 308, pp. 227–32.
97. X. Xiong and K. Ho: *J. Appl. Phys.*, 1995, vol. 77, pp. 2094–96.
98. K. Ho, X. Xiong, J. Zhi, and L. Cheng: *J. Appl. Phys.*, 1993, vol. 74, pp. 6788–90.